



Contents lists available at ScienceDirect

## Automation in Construction

journal homepage: [www.elsevier.com/locate/autcon](http://www.elsevier.com/locate/autcon)

## Underground structure defect detection and reconstruction using crosshole GPR and Bayesian waveform inversion

Hui Qin<sup>a,b,c</sup>, Xiongyao Xie<sup>a,b</sup>, Jasper A. Vrugt<sup>c,d,\*</sup>, Kun Zeng<sup>a,b</sup>, Gai Hong<sup>a,b</sup>

<sup>a</sup>Key Laboratory of Geotechnical & Underground Engineering of Ministry of Education, Tongji University, Shanghai 200092, China

<sup>b</sup>Department of Geotechnical Engineering, College of Civil Engineering, Tongji University, Shanghai 200092, China

<sup>c</sup>Department of Civil and Environmental Engineering, University of California Irvine, CA 92697-1075, USA

<sup>d</sup>Department of Earth Systems Science, University of California Irvine, CA 92697-1075, USA

### ARTICLE INFO

#### Article history:

Received 3 October 2015

Received in revised form 11 March 2016

Accepted 14 March 2016

Available online xxx

#### Keywords:

Underground structure

Defect

Crosshole ground-penetrating radar (GPR)

Waveform inversion

Bayesian inference

Markov chain Monte Carlo (MCMC)

Discrete cosine transform (DCT)

### ABSTRACT

Crosshole ground-penetrating radar (GPR) is a widely used measurement technique to help inspect the structural integrity of man-made underground structures, yet the resulting waveform and travel-time data can be difficult, complex and challenging to interpret. Here, we introduce the elements of a Bayesian inversion method for analyzing crosshole GPR data to guide detection of defects (weakness zones) in underground concrete structures. This framework uses as main building blocks the two-dimensional finite-difference time-domain (FDTD) simulator, the discrete cosine transform (DCT) method, and the DREAM<sub>(ZS)</sub> algorithm to reconstruct the relative permittivity field of an underground concrete structure from full-waveform GPR inversion. The FDTD simulator solves numerically Maxwell's equations in the time and space domain of the crosshole GPR experiment and simulates iteratively the electromagnetic (EM) waveforms. The DCT algorithm transforms the Cartesian parameterization to the frequency domain and reduces drastically the dimensionality of the parameter space by retaining only the low-frequency DCT-coefficients. Markov chain Monte Carlo (MCMC) simulation with the DREAM<sub>(ZS)</sub> algorithm is used to estimate the posterior distribution of the DCT-coefficients. The usefulness and applicability of the FDTD–DCT–DREAM<sub>(ZS)</sub> framework is demonstrated on a synthetic test example involving a unit square concrete structure with a small defect. Our results demonstrate that the proposed method successfully detects and locates defects in concrete structures. The inversion results appear rather insensitive to the noise level of the measured GPR waveforms, and the amount of data used (number of receiving antenna positions), as long as a sufficient number of measurements is available. The more DCT-coefficients that are used to characterize the concrete structure, the more accurate the results, yet the larger the posterior uncertainty of the reconstructed permittivity fields.

© 2016 Elsevier B.V. All rights reserved.

### 1. Introduction

Ground-penetrating radar (GPR) is a geophysical method that uses radar pulses to image the subsurface. This nondestructive method uses electromagnetic (EM) radiation in the microwave band (UHF/VHF frequencies) of the radio spectrum, and detects the reflected signals from subsurface structures. GPR can have applications in a variety of media, including rock, soil, ice, fresh water, pavements and has found widespread application and use in civil engineering to detect subsurface objects, changes in material properties, and voids and cracks [1]. Yet, for large civil structures such as giant dams, large pile foundations, and deep diaphragm walls, the EM

waves emitted by surface GPR may not penetrate sufficiently deep to warrant an accurate detection and description of underground structures [2,3]. Indeed, the high EM frequencies required for spatial resolution are subject to severe attenuation in the underground. Defects of underground structures such as cracks, voids, and weakness zones may not only jeopardize structural integrity and quality, but also be hazardous and affect safety.

Crosshole GPR has been developed within the field of hydrogeophysics to image rapidly the electrical properties viz. dielectric permittivity and electrical conductivity of the shallow subsurface as proxy for the distribution and amount of soil water [4,5]. This method uses a transmitting and receiving antenna which are placed next to each other in two adjacent boreholes several meters spaced apart [6]. The transmitting antenna emits high-frequency radio waves in the range of 10 MHz to 1 GHz which are received by the antenna in the adjacent borehole. When the transmitted

\* Corresponding author.

E-mail address: [jasper@uci.edu](mailto:jasper@uci.edu) (J. Vrugt).

electromagnetic wave encounters a diffractor (e.g. buried object) or a boundary between two materials with contrasting dielectric properties, it will be reflected, refracted or scattered back. This signal (waveform) that arrives at the receiving antenna thus stores important information about the structure and properties of the subsurface in-between the two antennas. By using multiple different vertical positions of the transmitter and receiver antennas a crosshole GPR data set is obtained which much better characterizes the subsurface than waveforms measured with surface GPR.

In the (hydro)geophysics literature two different methods are used for crosshole GPR profiling. In fixed-offset crosshole GPR the vertical movement of the transmitter and receiver is synchronized and both move at the same time from one depth to the next, providing a rapid yet more qualitative investigation of the subsurface. In multi-offset crosshole GPR the antennas move independently from each other, offering numerous GPR profiles of different angles for quantitative analysis of the volume between boreholes [7], but at the expense of additional operator training, equipment cost, field and analysis time, and CPU-requirements.

Here, we use multi-offset crosshole GPR to help detect defects in underground concrete structures. Such defects often turn into flow paths of water with dielectric permittivity that differs substantially from its surrounding area. These differences in permittivity are measured indirectly by the EM waves recorded by the receiving antenna, and this data is used herein to locate defects (voids, cracks) in underground concrete structures. The conductivity of the concrete can be estimated jointly as well but as this constitutes a fundamentally different material property it does not necessarily help us to extract information from the experimental data and guide the detection of structure defects. What is more, it would require increasing further the dimensionality of the parameter space.

The EM signals measured by the receiving antenna is not necessarily easy to interpret. Indeed, this signal requires numerical interpretation to determine the size, location, and shape of the defects in the concrete. This constitutes an inverse problem and reconstructs from the measured EM waves a map of the dielectric permittivity of the structure (subsurface). Commonly used inversion methods provide only a single realization (image) of the structure of interest [8–10]. This realization exhibits the closest match between the observed and simulated EM waves but does not appropriately communicate measurement and modeling uncertainties [11]. Indeed, this “best” image derived from deterministic inversion methods constitutes just one realization of an infinite space of solutions deemed feasible if modeling and data uncertainties are explicitly considered [12]. Probabilistic inversion methods allow for the treatment of different sources of error and return to the user an ensemble of solutions deemed statistically acceptable. Such methods can be formulated using either a measure theoretic or random variable approach, the first being the most formal and axiomatic definition of probability and preferred by theoreticians, and the latter more easy and practical to use and therefore favored by practitioners. Among these methods, Bayesian inference coupled with Markov chain Monte Carlo (MCMC) simulation has found widespread application and use in GPR inversion [6,13–20]. This approach results in a posterior parameter distribution and quantifies the uncertainty in the modeling results emerging from the model, observed data, likelihood function and prior distribution.

The measurement resolution and density and choice of forward model are of crucial importance in the inversion of crosshole GPR data. Underground structures tend to be resistive for EM waves, and the propagation velocity of GPR signals depends primarily on the dielectric permittivity of the medium [15,21]. Consequently, first-arrival travel times and a ray-based forward simulator are most often used to reconstruct the structure through inference of the model parameters [22]. This approach is computationally appealing (CPU-efficient) and enjoys widespread use due to its affordable modeling

errors. Despite this progress made, this method suffers several critical deficiencies [23]. First-arrival travel times summarize only a portion of the information contained in the measured GPR radiograms, and discard thereby potentially important details of the surface structure corrupting unnecessarily the uncertainty of the inversion results. What is more, the use of a ray-based model simplifies the EM wave propagation to straight or curved rays, which may bias the inversion results [19]. With continuous advances in digital computing, it is now possible to use wave-based models and full-waveform inversion. This approach much better extracts the information of the measured GPR data and can much more accurately simulate EM wave propagation, boundary conditions and antenna properties. This approach was first used in seismic inversion [24,25], then introduced to crosshole GPR inversion [26,27], and is an enormous improvement over ray-based inversion [5,6,28–35].

In this paper, we present a probabilistic inversion method to determine the relative permittivity distribution of underground structures from crosshole GPR waveform data. We use herein a two-dimensional finite-difference time-domain (FDTD) model to simulate the EM wave propagation for a 2D permittivity distribution characterized sparsely using the discrete cosine transform (DCT). The posterior distribution of the DCT-parameters is determined by fitting the FDTD model against the observed GPR traces using MCMC simulation with DREAM<sub>(ZS)</sub> method [17,36–38]. The DREAM<sub>(ZS)</sub> algorithm automatically tunes the scale and orientation of the proposal distribution during evolution of the Markov chains to their limiting distribution and therefore leads to high sampling efficiencies and a rapid convergence. We are especially concerned herein with the impact of the amount of GPR data, their measurement errors, and the number of retained DCT-coefficients on the inversion results. The results of our stochastic inversion with DREAM<sub>(ZS)</sub> are benchmarked against those derived from deterministic inversion. This paper concludes with a summary of the main findings.

## 2. Methodology

In this section we describe the methodology used herein to simulate the crosshole GPR waveforms and determine the relative permittivity distribution of the underground structure of interest using stochastic inversion. We first describe the different elements of our Bayesian inversion methodology, then discuss the DREAM<sub>(ZS)</sub> algorithm for statistical inference of the DCT-parameters that describe the permittivity distribution, followed by a description of the FDTD forward simulator, and conclude this section with an introduction to the DCT methodology.

### 2.1. Bayesian inversion framework

The inspection of the crosshole GPR method can be described with the following (process)-equation

$$\tilde{\mathbf{d}} = f(\mathbf{m}, \tilde{\mathbf{u}}) + \mathbf{e}, \quad (1)$$

where  $\tilde{\mathbf{d}}$  is a vector with measured GPR data,  $f(\cdot)$  is a (non)linear function (model) that describes (simulates) the physical relation between the model parameters,  $\mathbf{m}$  and model input,  $\tilde{\mathbf{u}}$  and measured data, and  $\mathbf{e}$  signifies a vector of measurement data errors. The model parameters in this study define the two-dimensional distribution of relative dielectric permittivities of the underground structure, and the model input is a set of EM signals emitted by the GPR transmitting antenna. The measured data consists of the measured waveforms recorded by the receiving antenna, and are used to determine the parameters  $\mathbf{m}$ . The physical relation,  $f(\cdot)$  is determined by Maxwell's equations which are solved for our concrete structure

using a two-dimensional FDTD simulator [39]. The tilde operator,  $\sim$  is used to denote measured entities.

The FDTD parameters,  $\mathbf{m}$  can generally not be derived from closed-form analytic solutions and inverse methods are required to determine their values from the measured GPR waveforms. In the Bayesian framework [40], model parameters are represented by probability density functions whose posterior distribution  $p(\mathbf{m}|\tilde{\mathbf{d}})$  can be derived from the data  $\tilde{\mathbf{d}}$  using Bayes' law

$$p(\mathbf{m}|\tilde{\mathbf{d}}) = \frac{p(\mathbf{m})p(\tilde{\mathbf{d}}|\mathbf{m})}{p(\tilde{\mathbf{d}})}, \quad (2)$$

where  $p(\mathbf{m})$  denotes the prior distribution of  $\mathbf{m}$ ,  $L(\mathbf{m}|\tilde{\mathbf{d}}) \equiv p(\tilde{\mathbf{d}}|\mathbf{m})$  denotes the likelihood function, and  $p(\tilde{\mathbf{d}})$  is a normalizing constant (probability density of  $\tilde{\mathbf{d}}$ ) that ensures that the posterior parameter distribution integrates to unity. We can discard probability density of  $\tilde{\mathbf{d}}$  or  $p(\tilde{\mathbf{d}})$  from Eq. (2) as all our inferences about the model parameters can be made from the unnormalized density

$$p(\mathbf{m}|\tilde{\mathbf{d}}) \propto p(\mathbf{m})L(\mathbf{m}|\tilde{\mathbf{d}}). \quad (3)$$

The prior probability density,  $p(\mathbf{m})$  describes, in a probabilistic sense, all our knowledge of the model parameters before collecting the experimental data,  $\tilde{\mathbf{d}}$ . In most investigations the spatial distribution of the dielectric permittivity of the medium under consideration is unknown and a uniform (noninformative/flat) prior distribution is used [41]. The main problem now resides in the formulation of the likelihood function,  $L(\mathbf{m}|\tilde{\mathbf{d}})$  used to summarize, in probabilistic terms, the level of agreement between the observed and FDTD simulated waveforms. If we conveniently assume the measurement errors,  $\mathbf{e}$  to be independent and normally distributed with constant variance,  $e \stackrel{D}{\sim} \mathcal{N}(0, \hat{\sigma}^2)$  then the likelihood function is given by

$$L(\mathbf{m}|\tilde{\mathbf{d}}, \hat{\sigma}^2) = \frac{1}{(\sqrt{2\pi}\sigma)^N} \exp\left(-\frac{1}{2} \sum_{i=1}^N \frac{(f_i(\mathbf{m}, \tilde{\mathbf{u}}) - \tilde{\mathbf{d}}_i)^2}{\hat{\sigma}^2}\right), \quad (4)$$

where  $\hat{\sigma}^2$  is the variance of the measurement data error, and  $N$  denotes the number of GPR observations, also called data points. For reasons of numerical stability and algebraic simplicity it is often convenient to work with the log-likelihood,  $\mathcal{L}(\mathbf{m}|\tilde{\mathbf{d}}, \hat{\sigma}^2)$  instead

$$\mathcal{L}(\mathbf{m}|\tilde{\mathbf{d}}, \hat{\sigma}^2) = -\frac{N}{2} \ln(2\pi) - \frac{N}{2} \ln(\hat{\sigma}^2) - \frac{1}{2} \hat{\sigma}^{-2} \text{SSE}(\mathbf{m}|\tilde{\mathbf{d}}, \tilde{\mathbf{u}}) \quad (5)$$

where SSE signifies the commonly used sum of squared errors

$$\text{SSE}(\mathbf{m}|\tilde{\mathbf{d}}, \tilde{\mathbf{u}}) = \sum_{i=1}^N (f_i(\mathbf{m}) - \tilde{\mathbf{d}}_i)^2. \quad (6)$$

in fitting (non)linear functions to data. The SSE term measures the difference between the observed and simulated GPR waveforms, and thus evaluates the performance of the model for given parameter values. The smaller the value of the SSE, the larger the value of the log-likelihood function, and thus the better the FDTD model fits the observed data. Note, we focus our attention herein on the relative permittivity of the concrete underground structure as this variable is sufficient to mimic the measured waveforms. The conductivity of the concrete can be estimated jointly as well but as this constitutes a fundamentally different material property it does not necessarily help us to extract information from the experimental data and guide the detection of structure defects. Also, it would require increasing further the dimensionality of the parameter vector.

Eq. (5) is rather simplistic in that it assumes a-priori that the error residuals are uncorrelated and Gaussian distributed with a constant

variance. This assumption might not be particularly realistic for the GPR waveform data. Errors in the FDTD model formulation and input data will corrupt the ability of the model to describe accurately the observed data, and introduce residuals errors that deviate considerably from normality. If the error residuals,  $\mathbf{e}(\mathbf{m}) = \tilde{\mathbf{d}} - f(\mathbf{m}, \tilde{\mathbf{u}}) = \{e_1(\mathbf{m}, \tilde{\mathbf{u}}), \dots, e_n(\mathbf{m}, \tilde{\mathbf{u}})\}$  exhibit temporal (or spatial) correlation then one can try to take explicit account of this in the derivation of the log-likelihood function. For instance, first-order correlation can be incorporated easily and leads to the following formulation of the log-likelihood function

$$\begin{aligned} \mathcal{L}(\mathbf{m}|\tilde{\mathbf{d}}, \tilde{\mathbf{u}}, \phi, \hat{\sigma}^2) = & -\frac{N}{2} \log(2\pi) + \frac{1}{2} \log(1 - \phi^2) \\ & - \frac{1}{2} (1 - \phi^2) \hat{\sigma}^{-2} e_1(\mathbf{m}, \tilde{\mathbf{u}})^2 - (N - 1) \log(\hat{\sigma}) \\ & - \frac{1}{2} \hat{\sigma}^{-2} \sum_{i=2}^n (e_i(\mathbf{m}, \tilde{\mathbf{u}}) - \phi e_{i-1}(\mathbf{m}, \tilde{\mathbf{u}}))^2, \end{aligned} \quad (7)$$

where  $|\phi| < 1$  signifies the first-order autoregressive coefficient, and the nuisance variables  $\{\phi, \sigma\}$  are subject to inference with the model parameters,  $\mathbf{m}$  using the observed data,  $\tilde{\mathbf{d}}$ . Alternative formulations of the likelihood function have been derived in the literature and can be used in cases where the error residuals are non-Gaussian with varying degrees of kurtosis and skewness. Latent variables can also be used to augment likelihood functions and take better consideration of forcing data and model structural error.

Once the prior distribution and likelihood function have been defined, what is left in Bayesian analysis is to summarize the posterior distribution, for example by the mean, the covariance or percentiles of individual parameters and/or nuisance variables. Unfortunately, the simulated waveforms of the FDTD model are dependent in a complex and nonlinear way on the prescribed permittivity distribution and EM waves emitted by the transmitter antenna, and this task cannot be carried out by analytical means nor by analytical approximation. Confidence intervals construed from a classical first-order approximation around the values of  $\mathbf{m}$  derived from deterministic inversion methods can then only provide an approximate estimate of the posterior distribution. We therefore resort to MCMC simulation with the DREAM<sub>(ZS)</sub> algorithm to generate a sample of the posterior distribution.

## 2.2. Markov chain Monte Carlo simulation: DREAM<sub>(ZS)</sub>

The basis of MCMC simulation is a Markov chain that generates a random walk through the search space and successively visits solutions with stable frequencies stemming from a stationary distribution,  $\tilde{\pi}(\cdot)$ . To explore the target distribution,  $\tilde{\pi}(\cdot)$ , a MCMC algorithm generates trial moves from the current state of the Markov chain  $\mathbf{m}_{t-1}$  to a new state  $\mathbf{m}_p$ . The earliest and most general MCMC approach is the random walk Metropolis (RWM) algorithm [42]. Assuming that a random walk has already sampled points  $\{\mathbf{m}_0, \dots, \mathbf{m}_{t-1}\}$  this algorithm proceeds in the following three steps. First, a candidate point  $\mathbf{m}_p$  is sampled from a proposal distribution  $q(\cdot)$  that is symmetric,  $q(\mathbf{m}_{t-1}, \mathbf{m}_p) = q(\mathbf{m}_p, \mathbf{m}_{t-1})$  and may depend on the present location,  $\mathbf{m}_{t-1}$ . Next, the candidate point is either accepted or rejected using the Metropolis acceptance probability [42].

$$p_{\text{acc}}(\mathbf{m}_{t-1} \rightarrow \mathbf{m}_p) = \min \left[ 1, \frac{p(\mathbf{m}_p)}{p(\mathbf{m}_{t-1})} \right], \quad (8)$$

where  $p(\cdot)$  denote the density of the target distribution (equivalent to Eq. (4)). If the proposal is accepted the chain moves to  $\mathbf{m}_t = \mathbf{m}_p$  otherwise the chain remains at its current location,  $\mathbf{m}_t = \mathbf{m}_{t-1}$ .

The DREAM<sub>(ZS)</sub> algorithm is a MCMC algorithm that has its roots within the DREAM [36,38] and DE-MC [36,43] algorithm and uses an adaptive proposal distribution,  $q(\cdot)$  which automatically tunes scale and orientation and therefore leads to high sampling efficiencies and a rapid convergence. In DREAM<sub>(ZS)</sub>,  $K$  different Markov chains are run simultaneously in parallel. If the state of a single chain is given by the  $n$ -vector  $\mathbf{m}$ , then at each generation  $t - 1$  the  $K$  chains in DREAM<sub>(ZS)</sub> define a population,  $\mathbf{M}$  which corresponds to a  $K \times n$  matrix, with each chain as a row. If  $A$  is a subset of  $n^*$ -dimensions of the original parameter space,  $\mathbb{R}^{n^*} \subseteq \mathbb{R}^n$ , then a jump,  $d\mathbf{M}^i$  in the  $i$ th chain,  $i = \{1, \dots, K\}$  at iteration  $t = \{2, \dots, T\}$  is calculated from a matrix  $\mathbf{Z}$  of size  $l \times d$  with thinned history of the  $K$  chains,  $\mathbf{Z} = \{\mathbf{z}^1, \dots, \mathbf{z}^l\}$  using differential evolution [44,45]

$$d\mathbf{M}_A^i = \zeta_{n^*} + (\mathbf{1}_{n^*} + \lambda_{n^*})\gamma_{(\delta, n^*)} \sum_{j=1}^{\delta} (\mathbf{z}_A^j - \mathbf{z}_A^i)$$

$$d\mathbf{M}_{\neq A}^i = 0, \tag{9}$$

where  $\gamma = 2.38/\sqrt{2\delta n^*}$  is the jump rate,  $\delta$  denotes the number of chain pairs used to generate the jump, and  $\mathbf{a}$  and  $\mathbf{b}$  are vectors consisting of  $2\delta K$  integers drawn without replacement from  $\{1, \dots, l\}$ . The values of  $\lambda$  and  $\zeta$  are sampled independently from  $\mathcal{U}_{d^*}(-c, c)$  and  $\mathcal{N}_{n^*}(0, c^*)$ , the multivariate uniform and normal distribution with, typically,  $c = 0.1$  and  $c^*$  small compared to the width of the target distribution,  $c^* = 10^{-6}$  say. The candidate point of chain  $i$  at iteration  $t$  then becomes

$$\mathbf{M}_p^i = \mathbf{M}^i + d\mathbf{M}^i, \tag{10}$$

and the Metropolis ratio of Eq. (8) is used to determine whether to accept this proposal or not. If  $p_{\text{acc}}(\mathbf{M}^i \rightarrow \mathbf{M}_p^i) \geq \mathcal{U}(0, 1)$  the candidate point is accepted and the  $i$ th chain moves to the new position, that is  $\mathbf{m}_t^i = \mathbf{M}_p^i$ , otherwise  $\mathbf{m}_t^i = \mathbf{m}_{t-1}^i$ . The default equation for  $\gamma$  should, for Gaussian and Student target distribution, result in optimal acceptance rates close to 0.44 for  $n = 1$ , 0.28 for  $n = 5$ , and 0.23 for large  $n$ .

The  $n^*$ -members of the subset  $A$  are sampled from the entries  $\{1, \dots, n\}$  (without replacement) and define the dimensions of the parameter space to be sampled by the proposal. This subspace spanned by  $A$  is construed in DREAM<sub>(ZS)</sub> with the help of a crossover operator. To enhance the diversity of the proposals created by DREAM<sub>(ZS)</sub>, the algorithm includes a mix of parallel direction and snooker jumps [36]. This snooker jump is depicted schematically in Fig. 14 of [46] and uses an adaptive step size. Details of the DREAM<sub>(ZS)</sub> algorithm have appeared in [17,36,38,46] and interested readers are referred to these publications for further details. It suffices here to say that the DREAM<sub>(ZS)</sub> has been benchmarked on many different test problems and its ability to automatically tune the scale and orientation of the proposal distribution leads to an excellent performance [19,20,47]. Unless stated differently, in all our calculations of DREAM<sub>(ZS)</sub> presented herein we use default values of the algorithmic variables.

### 2.3. Forward simulation

The propagation of EM waves through some medium is governed by the well-known Maxwell's equations that describe how electric and magnetic fields are generated and altered by each other and by charges and currents. In crosshole GPR surveys, the transmitting and receiving antennas are placed vertically in adjacent boreholes and the vertical component of the electric field is measured. The transverse magnetic (TM) mode of Maxwell's equations therefore suffices

to describe the GPR experiment [48–50] and these coupled partial differential equations are given by

$$\frac{\partial E_z}{\partial t} = \frac{1}{\varepsilon} \left( \frac{\partial H_y}{\partial x} - \frac{\partial H_x}{\partial y} - \sigma E_z \right) \tag{11}$$

$$\frac{\partial H_x}{\partial t} = -\frac{1}{\mu} \left( \frac{\partial E_z}{\partial y} + \sigma^* H_x \right) \tag{12}$$

$$\frac{\partial H_y}{\partial t} = \frac{1}{\mu} \left( \frac{\partial E_z}{\partial x} - \sigma^* H_y \right), \tag{13}$$

where  $E_z$  (Volts/m) is the  $z$  component of the electric field  $E$ ,  $H_x$  (Amperes/m) and  $H_y$  (Amperes/m) are the  $x$  and  $y$  components of the magnetic field  $H$ ,  $\varepsilon$  (Farads/m) signifies the dielectric permittivity,  $\mu$  (Henries/m) denotes the magnetic permeability,  $\sigma$  (Siemens/m) is the conductivity, and  $\sigma^*$  (Ohms/m) represents the magnetic loss. For simplicity, we usually solve for the relative dielectric permittivity,  $\varepsilon_r$ , which is the dielectric permittivity,  $\varepsilon$ , expressed as a ratio relative to the permittivity of vacuum,  $\varepsilon_0$  ( $\approx 8.85 \times 10^{-12}$  Farads/m).

Analytical solution of Eqs. (11)–(13) is very difficult, if not impossible, for most practical situations [51,52] and we therefore resort to 2D numerical simulation using the FDTD simulator developed by [53]. This simulator discretizes the partial derivatives of Maxwell's equations in space (2D Cartesian representation) and time using central differencing. The numerical solution is then obtained by solving in a leapfrog manner the resulting finite-difference equations [39] and this provides a simulated EM field for the geometry, physical parameters, boundary conditions, time step, excitation, and transmitter and receiver positions of our crosshole GPR experiment. The time-lapse values of  $E_z$  at each receiver position and time are subsequently derived from the FDTD model output (simulated waveforms).

### 2.4. Model parameter dimensionality reduction

Numerical solution of the FDTD model for our GPR experiment requires definition of the relative permittivity,  $\varepsilon_r$  for each discretized grid cell of our structure. These values define the simulated EM field and are subject to inference using the observed GPR data. In principle, we could treat each grid cell as a parameter with a different value of  $\varepsilon_r$ . This Cartesian parameterization would involve the inference of many thousands of unknowns, an inversion problem that is prohibitively difficult and CPU-demanding to solve with the DREAM<sub>(ZS)</sub> algorithm. We therefore use a much more efficient parameterization and describe the value of the relative permittivity,  $\varepsilon_r$  of each grid cell using the discrete cosine transform [54]. This transformation, hereafter referred to as DCT, is defined as follows

$$R_{ab} = \alpha_a \alpha_b \sum_{s=0}^{S-1} \sum_{w=0}^{W-1} Q_{sw} \cos\left(\frac{a(2s+1)\pi}{2S}\right) \cos\left(\frac{b(2w+1)\pi}{2W}\right), \tag{14}$$

where  $a$  and  $b$  denote the row and column number of the DCT coefficient-matrix,  $\mathbf{R}$  and the  $S \times W$  matrix  $\mathbf{Q}$  stores a map of discretized values of the relative permittivity of the spatial domain of interest and

$$\alpha_a = \begin{cases} \frac{1}{\sqrt{S}} & \text{if } a = 0 \\ \sqrt{\frac{2}{S}} & \text{if } 1 \leq a \leq S-1 \end{cases} \quad \alpha_b = \begin{cases} \frac{1}{\sqrt{W}} & \text{if } b = 0 \\ \sqrt{\frac{2}{W}} & \text{if } 1 \leq b \leq W-1 \end{cases}. \tag{15}$$

Closer inspection of Eq. (14) demonstrates that the size of matrix  $\mathbf{R}$  is exactly similar to that of  $\mathbf{Q}$ , and thus the standard DCT operation

does not reduce parameter dimensionality. Indeed, each coordinate of the matrix  $\mathbf{Q}$  with values of  $\varepsilon_r$  has its own DCT-coefficient. We can transform the matrix  $\mathbf{Q}$  from the space domain to the frequency domain using the DCT-coefficients stored in  $\mathbf{R}$ . The information of this transformation is concentrated in the lower-frequency DCT-coefficients. We can thus safely discard the higher-frequency DCT-coefficients without losing significant information about the spatial pattern of relative permittivity values. Those lower-frequency DCT-coefficients are retained and define the FDTD model parameters that will be estimated during inversion using the DREAM<sub>(ZS)</sub> algorithm. This approach significantly reduces the dimensionality of the search space [19,20,55] and has desirable advantages for stochastic inversion, in that (i) the resolution and separation of scales is explicitly defined, (ii) the transformation is orthogonal and close to the optimal Karhunen-Loève transform, (iii) the computational efficiency is high, (iv) the basis vectors depend only on the dimensionality of the model, and (v) the transformation is linear and operates with real parameter values [19].

To provide a better understanding of how the DCT method operates in practice, please consider Fig. 1a which shows the relative permittivity of a synthetic unit square structure with grid size of 0.02 m in the  $x$  and  $z$  directions. This model has a square-shaped defect (weakness zone) that has a significantly larger value of the relative permittivity,  $\varepsilon_r = 12$  compared to the surrounding concrete structure,  $\varepsilon_r = 9$ . If all grid cells were treated as an unknown parameter, then the inversion would involve the estimation of 2500 ( $50 \times 50$ ) different relative permittivity values. We now reconstruct this field using the DCT. We store the values of each grid cell in the matrix  $\mathbf{Q}$  and derive the  $S \times W$  matrix  $\mathbf{R}$  consisting of  $P$  DCT-coefficients using Eq. (14). This matrix  $\mathbf{R}$  is plotted in Fig. 1b and demonstrates that the information of the frequency domain reconstruction is stored in the DCT-coefficients in the upper-left corner. In the plots Figs. 1d–f we now demonstrate what happens to the reconstructed field if an increasing number of DCT-coefficients [Fig. 1d ( $P = 36$ ); Fig. 1e

( $P = 78$ ); Fig. 1f ( $P = 136$ )] is used for reconstruction of the original relative permittivity field. Discarded DCT-coefficients are set to zero. The  $\ell^2$ -norm (Euclidean distance between reconstructed field and true model) of each parameterization is plotted with a square in Fig. 1c.

The more DCT-coefficients are used, the lower the  $\ell^2$ -norm and the better the reconstruction of the true field of  $\varepsilon_r$  values. Indeed, the information of the original permittivity field is stored in just a few DCT-coefficients in the frequency domain. About 100 DCT-coefficients appear sufficient to characterize with high fidelity and accuracy the original permittivity field. This amounts to only 4% of the original parameter dimensionality if a standard Cartesian parameterization were used with individual values for each grid cell.

### 3. Deterministic inversion results

We now use the synthetic field of Fig. 1a and illustrate the results of a classic deterministic inversion algorithm. This method uses a straight ray-based forward model [22], and implements the simultaneous iterative reconstruction technique (SIRT) [56] to minimize the error residuals of the observed and simulated first-arrival travel times. As we are particularly interested in the effect of the number of data points and their measurement error on the inversion results, we use multi-offset profiling with  $11 \times 11$  (top row),  $11 \times 26$  (middle row), and  $11 \times 51$  (bottom row) transmitter–receiver antenna pairs, respectively. The antenna setup of the first measurement approach ( $11 \times 11$ ) is depicted graphically in Fig. 1a using red dots (left) and black triangles (right) for the eleven vertical positions of the transmitter and receiving antennas, respectively. The different columns of Fig. 2 display the results for noise-free data,  $\hat{\sigma} = 0$  (left column: Figs. 2a, d, g), white noise with  $\hat{\sigma} = 0.5$  (middle column: Figs. 2b, e, h) and  $\hat{\sigma} = 1$  nanosecond (right column: Figs. 2c, f, i).

The deterministic inversion method correctly resolves the location and shape of the defect if the measurement data are observed

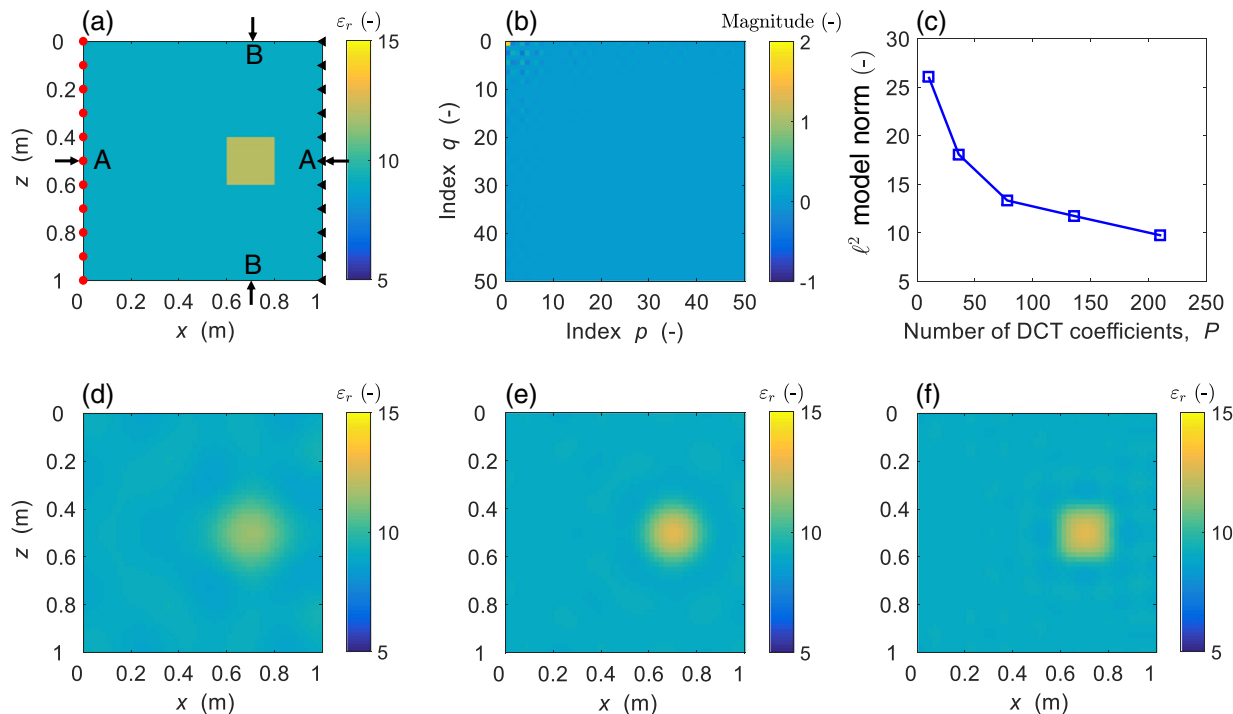


**Fig. 1.** Reconstruction of a synthetic relative permittivity field using the DCT: (a) true relatively permittivity field, (b)  $50 \times 50$  matrix  $\mathbf{R}$  consisting of  $P = 2500$  DCT-coefficients, (c)  $\ell^2$ -norm of reconstructed field for a different number of retained DCT-coefficients,  $P$ , and (d–f) realizations of the relative permittivity field using (d)  $P = 36$ , (e)  $P = 78$ , and (f)  $P = 136$  DCT-coefficients. The red dots and black triangles mark the vertical positions of the transmitter and receiving antennas, respectively as used in subsequent analysis. (For interpretation of the references to color in this figure legend, the reader is referred to the web version of this article.)

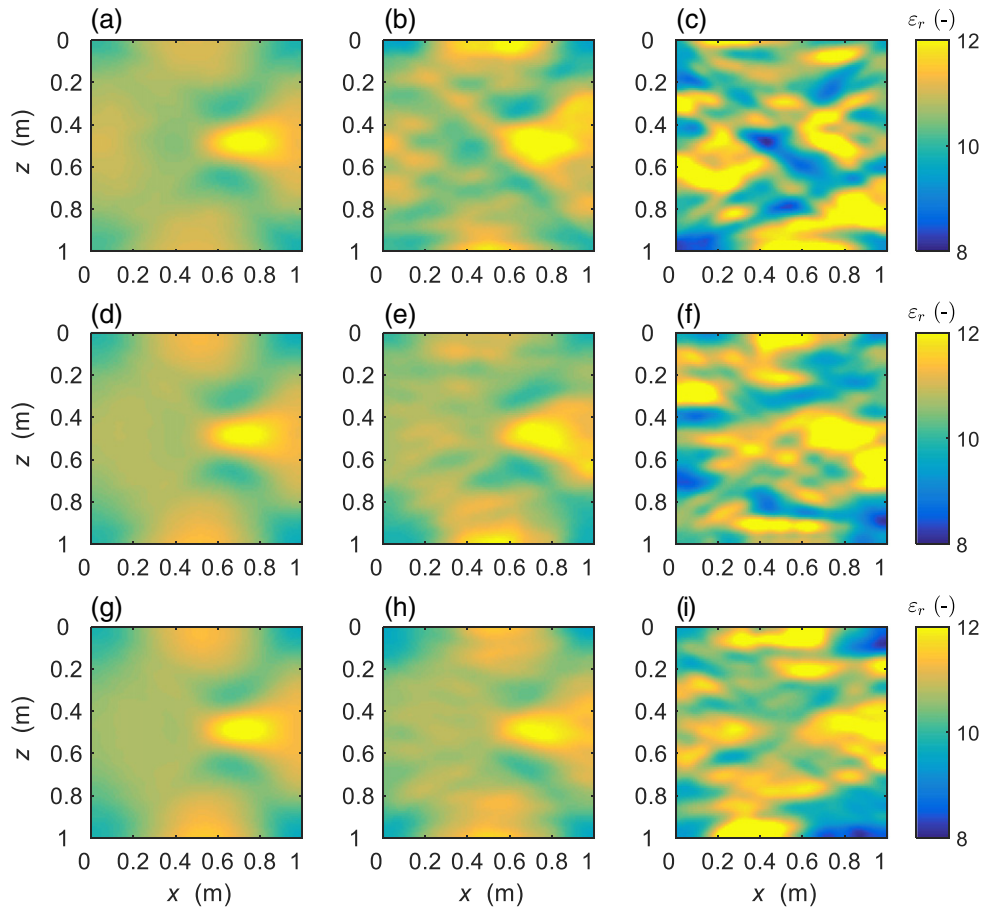


**Fig. 2.** Deterministic inversion of synthetic unit square field of relative permittivity values. The three different rows plot the results for a different number of data points used in the inversion and involve  $11 \times 11$  (top),  $11 \times 26$  (middle), and  $11 \times 51$  (bottom) antenna pairs. The three different columns depict the results for different white noise levels including  $\hat{\sigma} = 0$  (left),  $\hat{\sigma} = 0.5$  (middle) and  $\hat{\sigma} = 1$  (right) nanosecond.

with relatively little or no noise,  $\hat{\sigma} \leq 0.5$  (left and middle column). For larger values of the measurement data error, deterministic inversion can no longer pinpoint exactly the defect and instead incorrectly describes large parts of the domain as structurally weak. The inversion results are not particularly influenced by the number of data points (first-arrival travel times) as the three different panels appear very similar to each other.

#### 4. Bayesian inversion results

In this section, we use MCMC simulation with  $DREAM_{(ZS)}$  to estimate the posterior distribution of relative dielectric permittivity values used observations of synthetic waveforms. We specifically investigate the influence of the number of DCT-coefficients (model parameters), amount of data and their measurement error on the inversion results.

##### 4.1. Full waveform forward modeling

We take the synthetic relative permittivity model of Fig. 1a as our benchmark. Two boreholes separated 1 m apart and located at the left and right hand side of the unit square are used to create a synthetic record of GPR waveforms with the FDTD simulator. A total of eleven transmitting antennas (marked with red dots) are used in the left borehole, and  $J$  receiving antennas (black triangles) are placed in the adjacent borehole to the right to collect the GPR waveform data. Both antennas are varied over a distance of 1 m with

equidistant intervals of 10 cm. The EM source in our model, stored in the input variable,  $\hat{\mathbf{u}}$  (see Eq. (1)) is a Ricker wavelet with a central frequency of 500 MHz [57]. The EM pulses are emitted from the transmitting antenna and observed at positions where receiving antennas are placed. For each transmitter-receiver antenna pair, a 20 ns GPR trace is recorded with sampling interval of 0.047 ns. Thus, the observed data are comprised of  $11 \times J$  waveform traces with each trace consisting of 424 data points. We employ the GPRMAX2D implementation of the FDTD model [53] to carry out our forward simulations. To consider explicitly the effect of data uncertainty, we corrupt the observed GPR-waveform with a Gaussian measurement error using a fixed signal-to-noise ratio (SNR) to stabilize the noise level.

##### 4.2. Prior distributions of DCT-coefficients

MCMC simulation with the  $DREAM_{(ZS)}$  algorithm will resolve for the posterior distribution of the  $P$  retained DCT-coefficients. We sample the their in the log-transformed space and use a Jeffreys prior [58] for each DCT-coefficient to reflect a lack of knowledge of their appropriate values. The feasible range of the relative dielectric permittivity values is assumed to be [8–13] and models with one or more permittivity values outside this range are assigned a zero likelihood. We purposely adopt a relatively narrow range of relative permittivity values to accelerate convergence to the target distribution. Preliminary trials with  $DREAM_{(ZS)}$  with a much larger initial range of permittivity values (1–81) converged successfully to the target distribution but at the expense of a significantly increased computational cost.

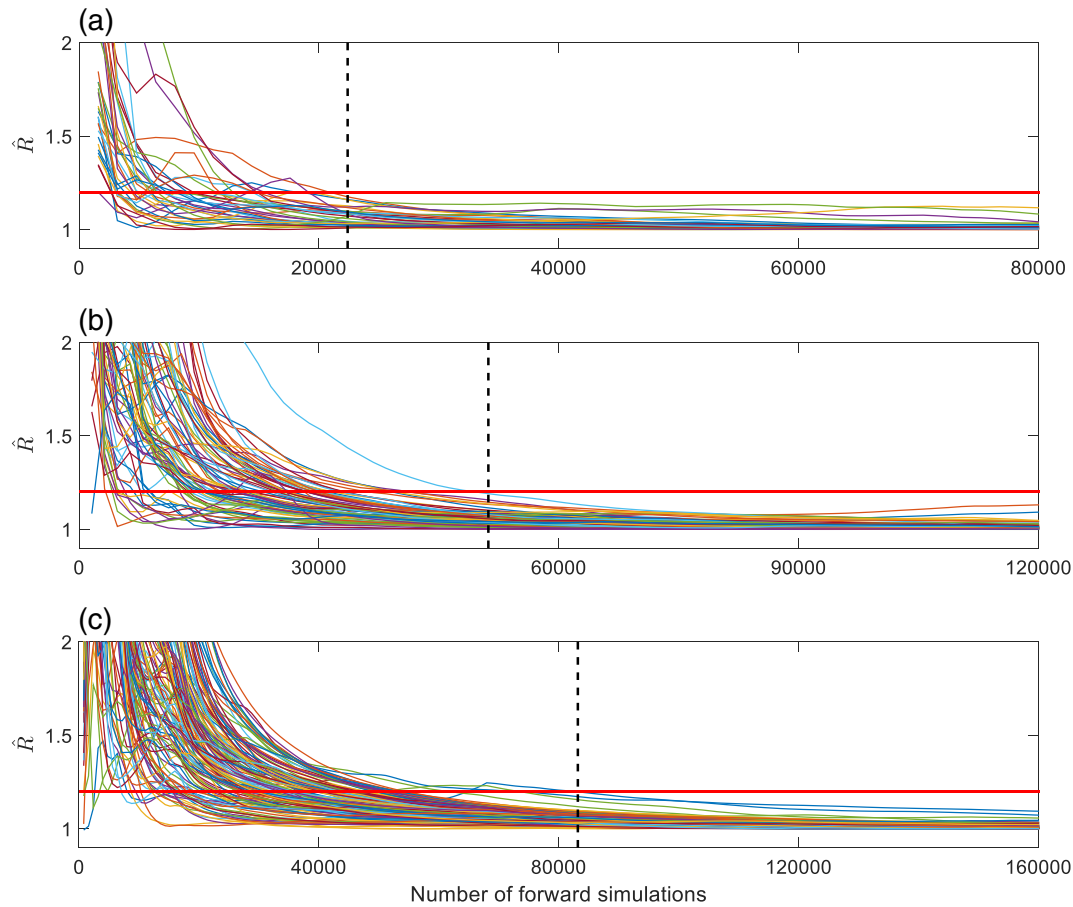


**Fig. 3.** Evolution of the  $\hat{R}$ -convergence diagnostic for three calibration cases involving (a)  $P = 36$ , (b)  $P = 78$ , and (c)  $P = 136$  DCT-coefficients. Each parameter is coded with a different color. The red horizontal line depicts the default threshold used to diagnose convergence to a limiting distribution, whereas the dotted black line (vertical) marks the number of FDTD model evaluations required to reach convergence. (For interpretation of the references to color in this figure legend, the reader is referred to the web version of this article.)

#### 4.3. $DREAM_{(ZS)}$ setup

To maximize computational efficiency, we used distributed computing and evaluate the  $K = 4$  Markov chains generated by  $DREAM_{(ZS)}$  on a different processor. We also increase the number of crossover values to 20 and use a value of  $\beta_0 = 1/4$  to decrease the jump rate to 25% of the default value and achieve a higher acceptance rate of proposals [46]. The  $\hat{R}$ -statistic of Gelman and Rubin [59] is used to monitor convergence of the sampled chain trajectories to a limiting distribution. This diagnostic compares for each parameter the within-chain and between-chain variance. A value of  $\hat{R}_j \leq 1.2$  for  $j = \{1, \dots, n\}$  diagnoses convergence to a limiting distribution, after which the last 50% of successively generated samples in each of the four chains can be used to approximate the posterior distribution.

#### 4.4. Inversion results: effect of number of DCT-coefficients

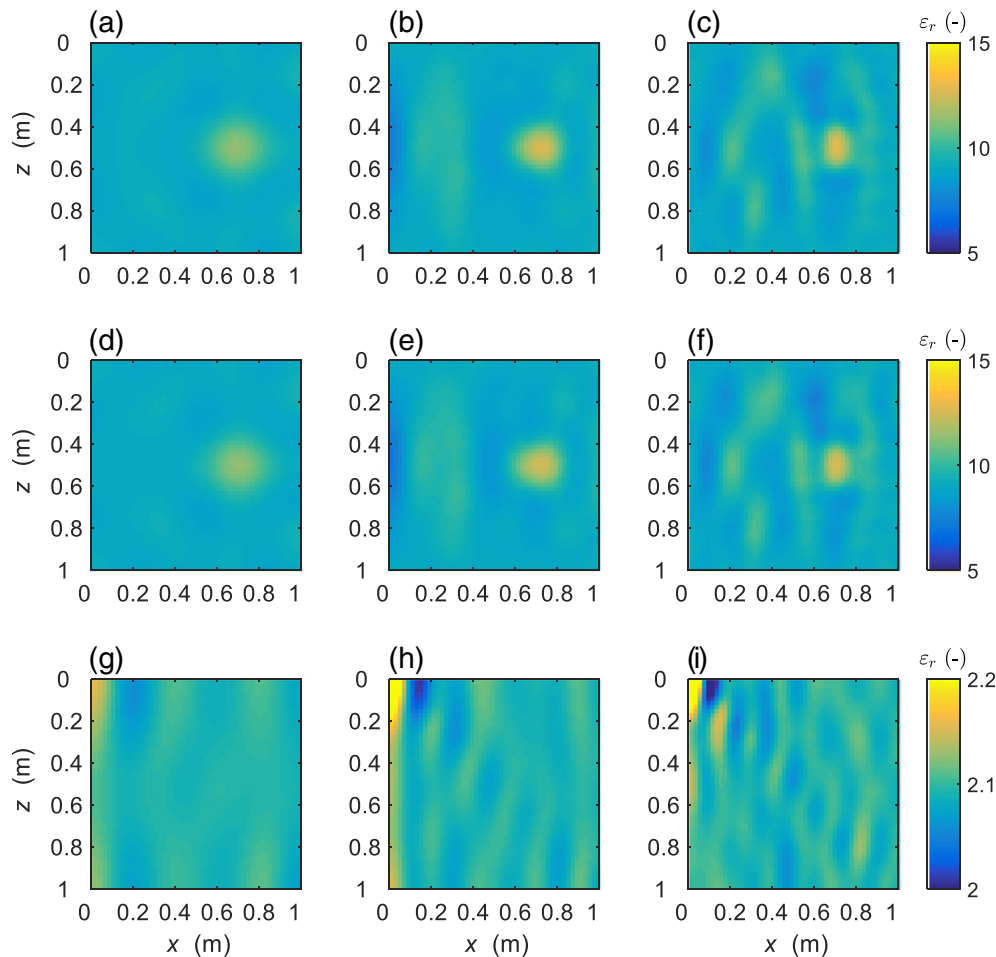
We now illustrate the results of our FDTD–DCT– $DREAM_{(ZS)}$  inversion approach using a total of  $P = 36$ ,  $P = 78$ , and  $P = 136$  DCT-coefficients. All these three cases reconstruct the original relative permittivity field from 561 ( $11 \times 51$ ) artificially generated GPR-waveforms which Gaussian (white noise) measurement error equivalent to  $SNR = 10$ .

Fig. 3 presents trace plots of the  $\hat{R}$ -convergence diagnostic for each of the  $P$  model parameters and three cases using the last 50% of the samples stored in each of the Markov chains. The different

parameters are color coded. Convergence to a stationary distribution can be declared if the  $\hat{R}_j$ -statistic of each of the  $P$  parameters drops below the critical value of 1.2. This threshold is indicated with the horizontal red line, whereas the black dotted vertical line marks the number of FDTD model evaluations required to officially reach convergence.

The larger the dimensionality of the parameter space the more iterations are needed with the  $DREAM_{(ZS)}$  algorithm to converge successfully to a limiting (posterior) distribution. For the three cases with (a: top)  $P = 36$ , (b: middle)  $P = 78$  and (c: bottom)  $P = 136$  parameters this equates to approximately 22000, 51000, and 83000 FDTD model evaluations.

We now resort our attention to the computational requirements of our Bayesian inversion method. This cost is determined almost entirely by the FDTD simulator as the vast majority of the CPU-time in our algorithm is spent on numerical solution of Maxwell equations to calculate the simulated waveform of each transmitter–receiver position for each vector of DCT-coefficients sampled by  $DREAM_{(ZS)}$ . As the required CPU-time is hardware (processor) dependent we adopt instead the notion of computational time unit (CTU) introduced by Laloy and Vrugt [17]. One CTU is equivalent to the CPU-time required to complete a single FDTD model evaluation. For the three cases considered herein, the total number of CTUs is equivalent to 22000, 51000 and 83000, respectively. Yet, as we run the  $K = 4$  chains in  $DREAM_{(ZS)}$  simultaneously in parallel, the actual number of CTUs is only one-fourth of their listed values for serial computation. On our computer this equates to a total CPU-time of 230, 530 and 870 min, respectively for each of the three



**Fig. 4.** Reconstructed relatively permittivity fields of the three different calibration cases involving (a,d)  $P = 36$ , (b,e)  $P = 78$ , and (c,f)  $P = 136$  DCT-coefficients. The top row plots the relatively permittivity field of the maximum a-posteriori (MAP) density solution of the posterior distribution, whereas the middle row displays the results of the posterior mean DCT-coefficients. The bottom panel plots the corresponding 95% credibility intervals derived from the posterior DCT-samples generated with the DREAM<sub>(ZS)</sub> algorithm.

case studies, as about 2.5 s are required for a single FDTD model simulation.

To provide better insights into the results of the different inversion trials, Fig. 4 plots for each of these three cases (as columns) the relatively permittivity fields of (a–c: top) the maximum a-posteriori (MAP) density solution and (d–f: middle) the mean solution of the posterior DCT-coefficient distribution. The bottom row displays the 95% credibility intervals of the posterior mean relatively permittivity fields.

The reconstructed fields of the MAP and posterior mean solution appear virtually identical to each other for all three different cases considered and correctly pinpoint the location and shape of the defect. In fact, the larger the number of DCT-coefficients that is used (right column) the more sharp the defect area (highest resolution) but also the more variation is observed in the relatively permittivity across the unit square structure. The more DCT-coefficients are retained the higher the resolution of the reconstructed field but at the expense of an increased uncertainty of the relatively permittivity values (bottom row). Thus, there is a trade-off between resolution and uncertainty.

We now compare the permittivity values of two different cross-sections of the unit square concrete structure. These cross-sections are depicted schematically in Fig. 1a and involve the transects A-A and B-B. Both these cross sections cut across the middle of the defect area but exhibit a different orientation. The A-A cross section is

horizontal and goes from left to right across the structure and defect. The B-B transect, on the contrary is vertically oriented. Fig. 5 presents the measured (red circles) and MAP simulated (blue crosses) relative permittivity values of the A-A (left column) and B-B (right column) transects for each of the three different calibration cases involving (top row)  $P = 36$ , (middle row),  $P = 78$  and (bottom row)  $P = 136$  retained DCT-coefficients. The 95% credibility intervals are separately indicated with the dotted black lines, and the gray region makes up the confidence intervals of the MAP simulated relatively permittivity values.

The three different calibration cases resolve accurately the structure defect so visible in the actual measured permittivity values (red circles). The use of  $P = 36$  DCT-coefficients appears sufficient to reasonably locate the location, shape, and size of the defect. The more DCT-coefficients that are used in the inversion the better the reconstruction of the permittivity discontinuity induced by the defect. The better the characterization of this sharp boundary between the defect and surrounding concrete the more wiggle and deviation from the measured permittivity values is introduced in the remaining part of the unit square concrete structure (e: bottom left). This variation (and error) is far less in the vertical B-B transect (f: bottom right). Indeed, the inversion accuracy is highest in the vertical direction. This is explained by the measurement design used to create the artificial data set of waveform observations, in which GPR signals are transmitted from left to right, providing more restrictions

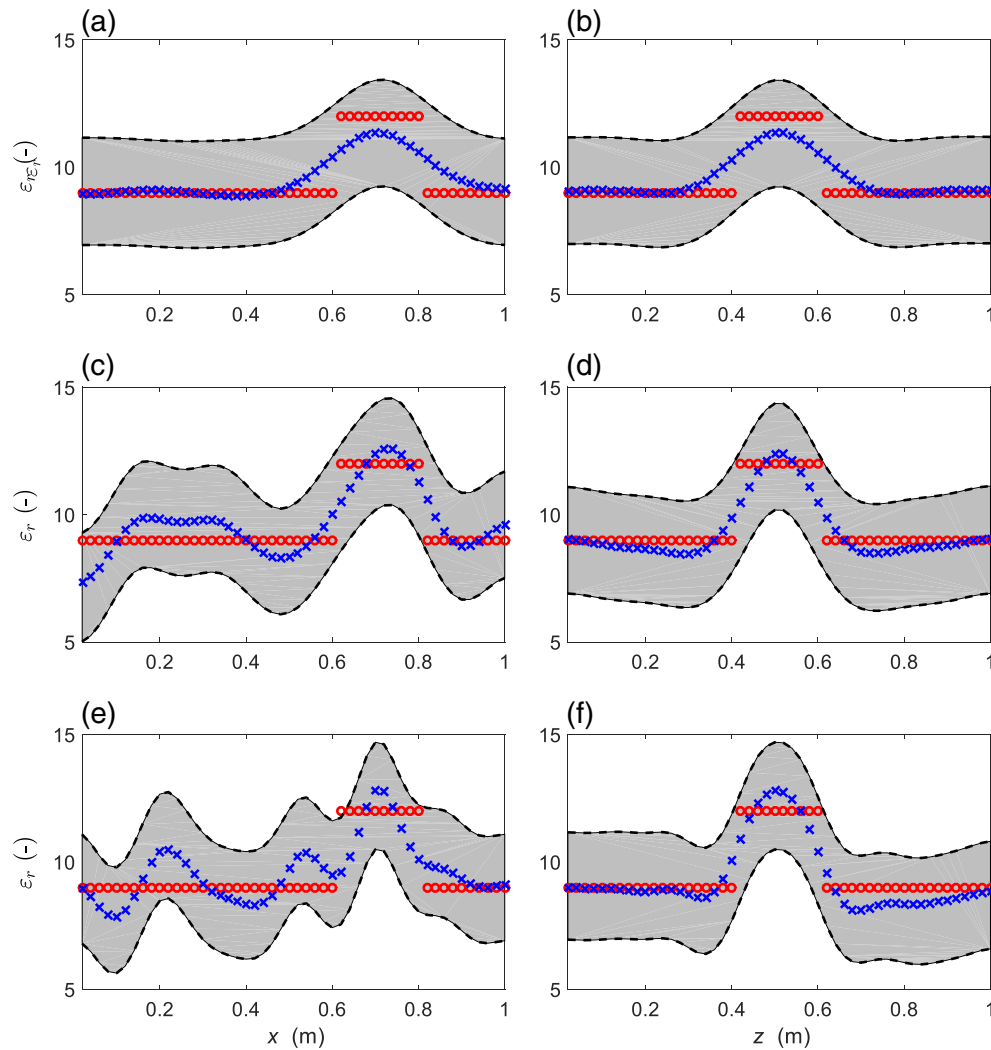


**Fig. 5.** Comparison of MAP simulated (blue crosses) and observed (red circles) permittivity values for the horizontal A–A (left column) and vertical B–B (right column) transect. The three different rows consider three different inversions with the DREAM<sub>(ZS)</sub> algorithm using (top row)  $P = 36$ , (middle row),  $P = 78$  and (bottom row)  $P = 136$  DCT-coefficients. The black dotted lines depict the 95% credibility intervals, and the gray region between the two lines signifies the confidence interval. (For interpretation of the references to color in this figure legend, the reader is referred to the web version of this article.)

vertically than horizontally. To improve the horizontal resolution we can include in the inversion with DREAM<sub>(ZS)</sub> surface-to-borehole data [60], yet this is beyond the scope of the present paper and will be explored in due course. The 95% credible region include almost all the observed permittivity values (all three inversion cases) with the exception of one observation in the bottom left plot when  $P = 136$  DCT-coefficients are used.

#### 4.5. Inversion results: effect of number of observations

In crosshole GPR surveys, the number of observations is often a trade-off between inversion accuracy and measurement cost. The larger the number of measurements used during the inversion, generally the more accurate the DCT-coefficients, and thus the more reliable the resolved structure and thus geophysical model. As continuous observation is impossible in geophysical explorations, it is necessary to determine an appropriate amount of observations, which satisfies the desired inversion accuracy and measurement budget.

To better understand how the inversion results depend on the number of measured GPR waveforms we consider three different calibration cases involving 11, 26 and 51 receiving antennas and

$P = 78$  DCT-coefficients (others are set to zero). Prior to the inversions, we perturb the synthetically generated waveforms of the FDTD model with white noise using  $\text{SNR} = 10$ . This corrupted GPR data set then serves as measurement data set in the subsequent inversions.

Fig. 6 plots for each of these three calibration cases (as columns) the relatively permittivity fields of (a–c: top) the MAP density solution and (d–f: middle) the mean solution of the posterior DCT-coefficient distribution. The bottom row displays the 95% credibility intervals of the posterior mean relatively permittivity fields.

As expected, the MAP and posterior mean realizations of the permittivity distribution of the concrete structure are getting better with an increasing number of measurements used in the inversion (compare a–c and d–f). The 95% credibility intervals in the bottom row appear very similar, demonstrating that the number of GPR waveforms has relatively little effect on the posterior uncertainty of the DCT-coefficients.

Fig. 7 quantifies the impact of the amount of GPR data on the accuracy of the inversion results, and plots the  $\ell^2$ -norm of the MAP (blue square) and posterior mean (red triangle) reconstructed relative permittivity values and their measured field values.

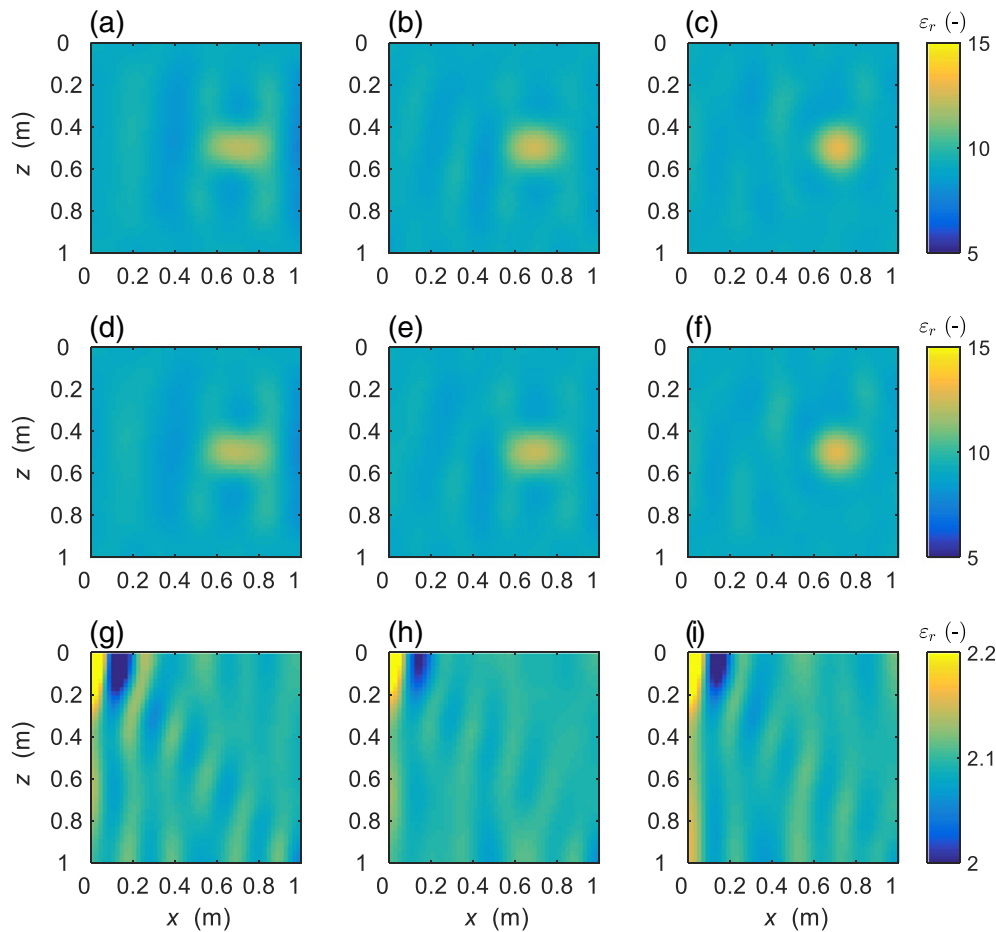


**Fig. 6.** Reconstructed relatively permittivity fields of the three different calibration cases (left to right) involving (a,d)  $11 \times 11$ , (b,e)  $11 \times 26$ , and (c,f)  $11 \times 51$  waveform observations. The top row plots the relatively permittivity field of the MAP density solution of the posterior distribution, whereas the middle row displays the results of the posterior mean DCT-coefficients. The bottom panel plots the corresponding 95% credibility intervals derived from the posterior DCT-samples generated with the DREAM<sub>(ZS)</sub> algorithm.

The three different calibration cases are listed along the  $x$ -axis and involve the use of 11, 26 and 51 receiving antennas. The norm traces of the MAP and posterior mean solution are in close agreement with each other similar and demonstrate an improved accuracy of the reconstructed permittivity fields when the number of receiving antennas (observations) is increased. When the number of receiving antennas increases from 11 to 26, the  $\ell^2$ -norm decreases from 25.1 to 19.1 for the MAP solution, and from 26.0 to 20.9 for the posterior mean estimates of the DCT-coefficients. In all three cases considered herein, the MAP estimate is a slightly better predictor of the true permittivity field than its counterpart derived from the posterior mean solution sampled with the DREAM<sub>(ZS)</sub> algorithm.

For convenience, we define a simple metric called indicator or IND which quantifies the added benefits of one additional receiver antenna. This metric is easily calculated from the data presented in Fig. 7 and for the first leg is computed as  $IND_{MAP} = (25.1 - 19.1)/(26 - 11) = 0.40$  for the MAP solution, and  $IND_{mean} = 0.34$  for the posterior mean DCT-coefficients. This value of IND reduces to  $IND_{MAP} = 0.07$  and  $IND_{mean} = 0.10$  when the number of receiving antennas is increased further from 26 to 51. This simple analysis demonstrates that the added benefit of additional waveform data depends critically on the actual size of the GPR data set. If the GPR data set is relatively small, then one additional receiving antenna can enhance considerably the accuracy of the reconstructed permittivity field. The added benefit decreases with increasing number of receiving antennas being used.

#### 4.6. Inversion results: effect of measurement data errors

Various error sources inside and outside the GPR system contribute to measurement uncertainty of the recorded waveform. For instance, the internal device of the GPR may generate noisy signals. Moreover, environmental EM sources such as FM radios, televisions, and cellular phones, may enter the GPR system and interfere with GPR surveys [61,62]. System (systematic) errors can be eliminated in large part by local calibration, but random errors cannot be resolved and therefore remain present in the measured waveforms.

To evaluate the effect of GPR data measurement errors on the accuracy and reliability of the inversion results, we corrupt the FDTD simulated waveforms with three different (Gaussian) noise levels, including low-noise (SNR = 15), medium-noise (SNR = 10), and high-noise (SNR = 5). Fig. 8 displays the effect of this measurement error corruption on the measured waveform. The top plot (a) summarizes the original noise-free waveform, and the subsequent three panels plot the waveform with (b) low, (c) medium and (d) high noise.

The DREAM<sub>(ZS)</sub> inversion trials for the three different noise levels are depicted graphically in Fig. 9 using  $P = 78$  DCT-coefficient and  $11 \times 26$  antenna pairs. The first two rows plot the relatively permittivity fields of (a–c: top) the MAP density solution and (d–f: middle) the mean solution of the posterior DCT-coefficient distribution. The bottom row displays the 95% credibility intervals of the posterior mean relatively permittivity fields.

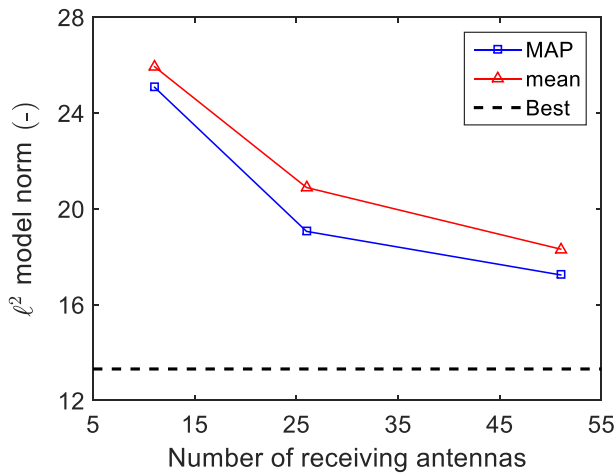


**Fig. 7.** Information content of GPR waveform data: trace plot of the  $\ell^2$ -norm between the observed and reconstructed relative permittivity fields of the MAP (blue squares) and posterior mean (red triangles) DCT-coefficients. The dotted black line denotes the performance of the best attainable permittivity field obtained without truncation of DCT-coefficient. (For interpretation of the references to color in this figure legend, the reader is referred to the web version of this article.)

The inversion results are hardly affected by the noise level. The MAP and posterior mean fields are in excellent agreement with the measured permittivity field and appear very similar to each other (different columns). The location, shape, and size of the defect is well resolved in all cases. Whereas the MAP and posterior mean DCT-solution appear unaffected by noise level, the posterior uncertainty increases with increasing size of the measurement data error. This is an expected result – the larger the measurement error, the more flat the likelihood function and thus the more spread out the probability mass over the DCT-coefficient space.

These findings confirm the ability of the DREAM<sub>(ZS)</sub> algorithm to traverse efficiently high-dimensional parameter spaces in pursuit of the posterior distribution of the DCT-coefficients. Deterministic waveform inversion methods use optimization principles to seek iterative improvement of the initial parameter estimates, and their performance is therefore strongly controlled by the properties of the response surface. Their search capabilities will deteriorate rapidly in

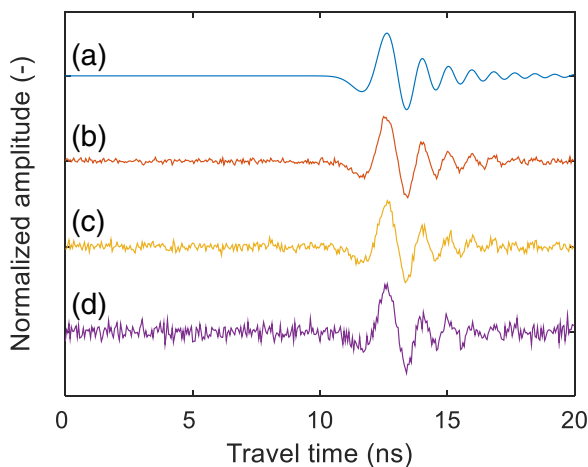


**Fig. 8.** Effect of measurement data errors on the measured waveform. The FDTD simulated waveform is corrupted with (a: blue) no-noise, (b: red) low-noise, (c: yellow) medium-noise, and (d: purple) high-noise. (For interpretation of the references to color in this figure legend, the reader is referred to the web version of this article.)

higher dimensions and lead to premature convergence when confronted with non-smooth search landscapes and local optima. The search capabilities of the DREAM<sub>(ZS)</sub> algorithm on the contrary are not as much affected by the properties of the response surface and model parameter dimensionality. Indeed, the proposal distribution of Eq. (10) is highly efficient in that it automatically detects the orientation and scale of the posterior distribution. What is more, the Metropolis ratio of Eq. (8) allows for the temporary acceptance of inferior (downhill) solutions, which enables DREAM<sub>(ZS)</sub> to escape from local optima.

We conclude our numerical experiments in Fig. 10 with a histogram of the posterior root-mean-square error (RMSE) values derived for the different noise levels. The sampled RMSE values are in close agreement with the SNR values used to corrupt the synthetic observations of the GPR waveform. This provides further evidence for the claim that the MAP and posterior mean DCT-solutions derived from MCMC simulation with the DREAM<sub>(ZS)</sub> algorithm fit the observed relatively permittivity field very well.

This concludes our manuscript. Future work will apply the FDTD–DCT–DREAM<sub>(ZS)</sub> framework to waveforms measured in real-world GPR-surveys. This is a necessary next step to validate the suitability and practical applicability of probabilistic inversion to defect detection in underground structures. Another logical step would be to extend the present framework to three-dimensional structures. This will be the subject of our subsequent work and will be reported in due course.

## 5. Summary and conclusions

In this paper we have introduced the different elements of a Bayesian inversion method for detection of defects in two-dimensional underground structures. This framework uses as main building blocks the two-dimensional FDTD simulator of Giannopoulos [53], the DCT method of Ahmed [54] and the DREAM<sub>(ZS)</sub> algorithm of ter Braak and Vrugt [17,36–38] to reconstruct the permittivity field of an underground concrete structure from full-waveform GPR inversion. The FDTD simulator solves numerically Maxwell's equations in the time and space domain of the experiment and simulates iteratively the GPR-waveforms for a given geometry, experimental setup, physical parameters, and other input data. The DCT algorithm transforms the Cartesian parameterization to the frequency domain and reduces drastically the dimensionality of the parameter space by retaining only the high-frequency DCT-coefficients. MCMC simulation with the DREAM<sub>(ZS)</sub> algorithm is used to estimate the posterior distribution of the DCT-coefficients.

The usefulness and applicability of the FDTD–DCT–DREAM<sub>(ZS)</sub> framework is demonstrated on a synthetic test example involving a unit square underground concrete structure with a small defect. A synthetic data set of GPR waveforms was simulated for this structure using two adjacent boreholes 1 m apart with a transmitter and receiver antenna. Several numerical experiments were performed to benchmark the methodology and determine how the accuracy and reliability of the inversion results (and reconstructed relative permittivity fields) depends on the amount of GPR-data, their measurement errors, and the number of DCT-coefficients.

Our results demonstrate that the proposed framework successfully resolves the measured permittivity field. The inferred location, shape and size of the defect is in excellent agreement with its true properties. The accuracy of the reconstructed permittivity field increases with the use of more DCT-coefficients in the inversion with DREAM<sub>(ZS)</sub>. The larger the number of DCT-coefficients that is retained during the inversion the higher the resolution of the posterior mean and MAP permittivity field, yet at the expense of an increased posterior uncertainty (larger 95% credibility regions). Inversions with different signal-to-noise ratios (SNR) demonstrate that larger measurement errors of the GPR-waveform do not affect the accuracy

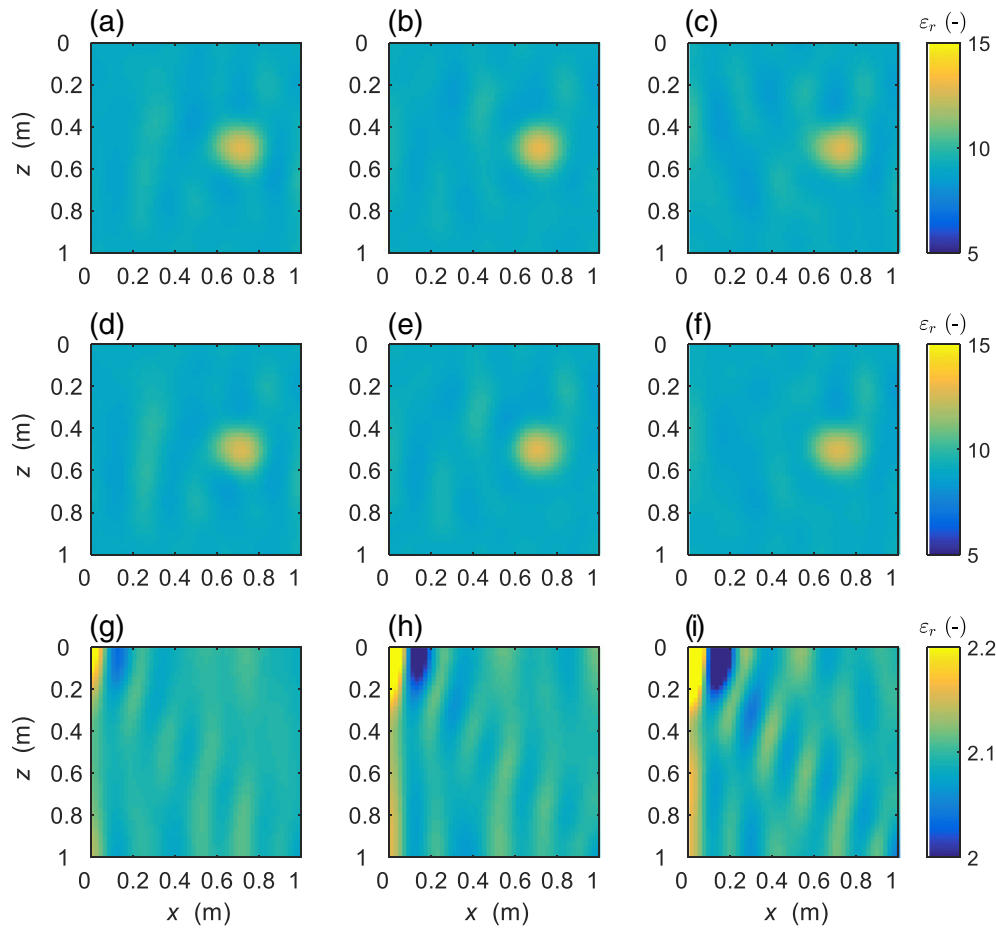


**Fig. 9.** Reconstructed relatively permittivity fields derived from the measured GPR-waveforms with (a,d) low-noise, (b,e) medium-noise, and (c,f) high-noise. The top row plots the relatively permittivity field of the MAP density solution of the posterior distribution, whereas the middle row displays the results of the posterior mean DCT-coefficients. The bottom panel plots the corresponding 95% credibility intervals derived from the posterior DCT-samples generated with the  $DREAM_{(zS)}$  algorithm.

and reliability of the reconstructed permittivity fields. A lower SNR only increases significantly the posterior uncertainty of the DCT-coefficients and the reconstructed fields. The amount of data has a significant effect on the inversion results if a relatively small number of receiver antennas is used, but the added value of new data diminishes rapidly with increasing size of the GPR-data set.

Future work will apply the FDTD–DCT– $DREAM_{(zS)}$  framework to waveforms measured in real-world GPR-surveys and consider

simulation and inference of three-dimensional structures. This work will be reported in due course.

#### Acknowledgments

The first author acknowledges support of the National Basic Research Program of China (973 Program: 2011CB013803), Natural Science Foundation of China (41372273), Shanghai Science and

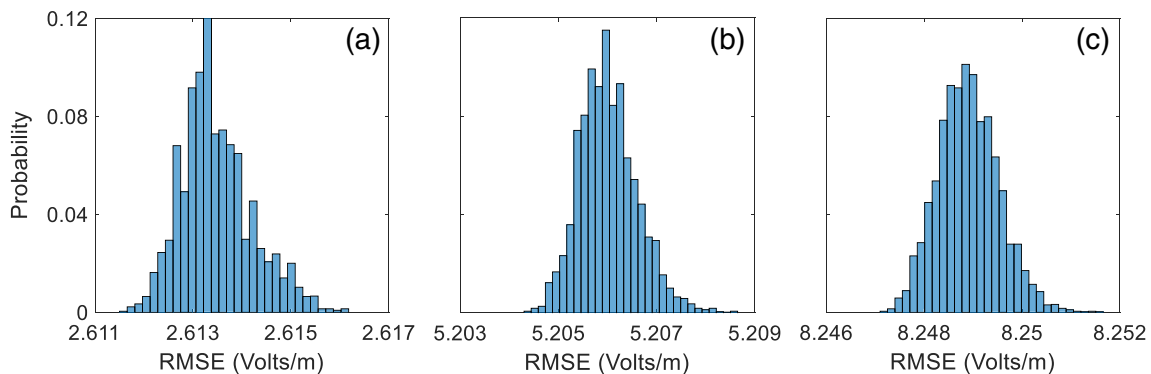


**Fig. 10.** Histograms of the RMSE values of the posterior solutions sampled with the  $DREAM_{(zS)}$  algorithm using observed waveforms with (a) low-noise:  $SNR = 15$ , (b) medium-noise:  $SNR = 10$ , and (c) high-noise:  $SNR = 5$ .

Technology Development Funds (12231200900, 13231200102), and the China Scholarship Council (201406260113).

## References

- [1] D.J. Daniels, *Ground Penetrating Radar*, Second edition ed., Institution of Engineering and Technology 2004.
- [2] P. Szymczyk, M. Szymczyk, Non-destructive building investigation through analysis of GPR signal by S-transform, *Autom. Constr.* 55 (2015) 35–46.
- [3] S. Li, H. Cai, V.R. Kamat, Uncertainty-aware geospatial system for mapping and visualizing underground utilities, *Autom. Constr.* 55 (2015) 105–119.
- [4] A.C. Hinnell, T.P.A. Ferr, J.A. Vrugt, J.A. Huisman, S. Moysey, J. Rings, M.B. Kowalsky, Improved extraction of hydrologic information from geophysical data through coupled hydrogeophysical inversion, *Water Resour. Res.* 46 (2010) W00D40
- [5] A. Klotszche, J. van der Kruk, G.A. Meles, J. Doetsch, H. Maurer, N. Linde, Full-waveform inversion of cross-hole ground-penetrating radar data to characterize a gravel aquifer close to the Thur River, Switzerland, *Near Surface Geophysics* 8 (2010) 635–649.
- [6] K.S. Cordua, T.M. Hansen, K. Mosegaard, Monte Carlo full-waveform inversion of crosshole GPR data using multiple-point geostatistical a priori information, *Geophysics* 77 (2012) H19–H31.
- [7] M.J. Harry, (Ed.), *Ground Penetrating Radar: Theory and Applications*, Elsevier 2009.
- [8] A.V. Lakshminarayanan, A. Lent, Methods of least squares and SIRT in reconstruction, *J. Theor. Biol.* 76 (1979) 267–295.
- [9] A. Tarantola, B. Valette, Generalized nonlinear inverse problems solved using the least squares criterion, *Rev. Geophys.* 20 (1982) 219–232.
- [10] J. Trampert, J.-J. Leveque, Simultaneous iterative reconstruction technique: physical interpretation based on the generalized least squares solution, *J. Geophys. Res.* Solid Earth 95 (1990) 12553–12559.
- [11] E. Slob, Uncertainty in ground penetrating radar models, 13th International Conference on Ground Penetrating Radar, 2010. pp. 1–5.
- [12] W. Trainor-Guitton, G.M. Hoversten, Stochastic inversion for electromagnetic geophysics: practical challenges and improving convergence efficiency, *Geophysics* 76 (2011) F373–F386.
- [13] K. Mosegaard, A. Tarantola, Monte Carlo sampling of solutions to inverse problems, *J. Geophys. Res.* 100 (1995) 12431–12447.
- [14] N. Linde, A. Binley, A. Tryggvason, L.B. Pedersen, A. Revil, Improved hydrogeophysical characterization using joint inversion of cross-hole electrical resistance and ground-penetrating radar traveltimes data, *Water Resour. Res.* 42 (2006) W12404
- [15] J. Bikowski, J.A. Huisman, J.A. Vrugt, H. Vereecken, J. van der Kruk, Integrated analysis of waveguide dispersed GPR pulses using deterministic and Bayesian inversion methods, *Near Surface Geophysics* 10 (2012) 641–652.
- [16] B. Dafflon, W. Barrash, Three-dimensional stochastic estimation of porosity distribution: benefits of using ground-penetrating radar velocity tomograms in simulated-annealing-based or Bayesian sequential simulation approaches, *Water Resour. Res.* 48 (2012) 1–13.
- [17] E. Laloy, N. Linde, J.A. Vrugt, Mass conservative three-dimensional water tracer distribution from Markov chain Monte Carlo inversion of time-lapse ground-penetrating radar data, *Water Resour. Res.* 48 (2012) 1–15.
- [18] M. Scholer, J. Irving, M.C. Looms, L. Nielsen, K. Holliger, Bayesian Markov-chain-Monte-Carlo inversion of time-lapse crosshole GPR data to characterize the vadose zone at the Arrenæs Site, Denmark, *Vadose Zone J.* 11 (2012) 1–19.
- [19] N. Linde, J.A. Vrugt, Distributed soil moisture from crosshole ground-penetrating radar travel times using stochastic inversion, *Vadose Zone J.* 12 (2013) 1–16.
- [20] T. Lochbühler, J.A. Vrugt, M. Sadegh, N. Linde, Summary statistics from training images as prior information in probabilistic inversion, *Geophys. J. Int.* 201 (2015) 157–171.
- [21] T.J. Heimovaara, J.A. Huisman, J.A. Vrugt, W. Bouten, Obtaining the spatial distribution of water content along a TDR probe using the SCEM-UA Bayesian inverse modeling scheme, *Vadose Zone J.* 3 (2004) 1128–1145.
- [22] K.A. Dines, R.J. Lytle, Computerized geophysical tomography, *Proceedings of the IEEE*, 67, 1979. pp. 1065–1073.
- [23] P.R. Williamson, M.H. Worthington, Resolution limits in ray tomography due to wave behavior: Numerical experiments, *Geophysics* 58 (1993) 727–735.
- [24] A. Tarantola, Inversion of seismic reflection data in the acoustic approximation, *Geophysics* 49 (1984) 1259–1266.
- [25] A. Tarantola, A strategy for nonlinear elastic inversion of seismic reflection data, *Geophysics* 51 (1986) 1893–1903.
- [26] J.R. Ernst, A.G. Green, H. Maurer, Klaus. Holliger, Application of a new 2D time-domain full-waveform inversion scheme to crosshole radar data, *Geophysics* 72 (2007) J53–J64.
- [27] J.R. Ernst, H. Maurer, A.G. Green, K. Holliger, Full-waveform inversion of crosshole radar data based on 2-D finite-difference time-domain solutions of Maxwell's equations, *IEEE Transactions on Geoscience and Remote Sensing*, 45, 2007. pp. 2807–2828.
- [28] A. Kalogeropoulos, J. van der Kruk, J. Huggenschmidt, S. Busch, K. Merz, Chlorides and moisture assessment in concrete by GPR full waveform inversion, *Near Surface Geophysics*, 9, 2011. pp. 277–285.
- [29] G.A. Meles, S.A. Greenhalgh, A.G. Green, H. Maurer, J. van der Kruk, GPR full-waveform sensitivity and resolution analysis using an FDTD adjoint method, *IEEE Transactions on Geoscience and Remote Sensing*, 50, 2012. pp. 1881–1896.
- [30] A. Klotszche, J. van der Kruk, N. Linde, J. Doetsch, H. Vereecken, 3-D characterization of high-permeability zones in a gravel aquifer using 2-D crosshole GPR full-waveform inversion and waveguide detection, *Geophys. J. Int.* 159 (2013) 932–944.
- [31] A. Kalogeropoulos, J. van der Kruk, J. Huggenschmidt, J.B.E. Brhwiler, Full-waveform GPR inversion to assess chloride gradients in concrete, *NDT & E Int.* 57 (2013) 74–84.
- [32] M. Oberrohrmann, A. Klotszche, H. Vereecken, J. van der Kruk, Optimization of acquisition setup for cross-hole GPR full-waveform inversion using checkerboard analysis, *Near Surface Geophysics*, 11, 2013. pp. 197–209.
- [33] X. Yang, A. Klotszche, G. Meles, H. Vereecken, J. van der Kruk, Improvements in crosshole GPR full-waveform inversion and application on data measured at the Boise Hydrogeophysics Research Site, *J. Appl. Geophys.* 99 (2013) 114–124.
- [34] S. Busch, J. van der Kruk, H. Vereecken, Improved characterization of fine-texture soils using on-ground GPR full-waveform inversion, *IEEE Transactions on Geoscience and Remote Sensing*, 52, 2014. pp. 3947–3958.
- [35] N. Gueting, A. Klotszche, J. van der Kruk, J. Vanderborght, H. Vereecken, A. Englert, Imaging and characterization of facies heterogeneity in an alluvial aquifer using GPR full-waveform inversion and cone penetration tests, *J. Hydrol.* 524 (2015) 680–695.
- [36] C.J.F. ter Braak, J.A. Vrugt, Differential evolution Markov chain with snooker updater and fewer chains, *Stat. Comput.* 18 (2008) 435–446.
- [37] J.A. Vrugt, P.H. Stauffer, T. Whiting, B.A. Robinson, V.V. Vesselinov, Inverse modeling of subsurface flow and transport properties: a review with new developments, *Vadose Zone J.* 7 (2008) 843–864.
- [38] J.A. Vrugt, C.J.F. ter Braak, C.G.H. Diks, B.A. Robinson, J.M. Hyman, D. Higdon, Accelerating Markov chain Monte Carlo simulation by differential evolution with self-adaptive randomized subspace sampling, *Int. J. Non Linear Sci. Numer. Simul.* 10 (2009) 271–288.
- [39] K.S. Yee, Numerical solution of initial boundary value problems involving Maxwell's equations in isotropic media, *IEEE Transactions on Antennas and Propagation*, AP-14, 1966. pp. 302–307.
- [40] A. Tarantola, B. Valette, Inverse problems = quest for information, *J. Geophys.* 50 (1982) 159–170.
- [41] M. Rosas-Carbajal, N. Linde, T. Kalscheuer, J.A. Vrugt, Two-dimensional probabilistic inversion of plane-wave electromagnetic data: methodology, model constraints and joint inversion with electrical resistivity data, *Geophys. J. Int.* 193 (2014) 1508–1524.
- [42] N. Metropolis, A.W. Rosenbluth, M.N. Rosenbluth, A.H. Teller, E. Teller, Equation of state calculations by fast computing machines, *J. Chem. Phys.* 21 (1953) 1087–1092.
- [43] C.J.F. ter Braak, A Markov chain Monte Carlo version of the genetic algorithm differential evolution: easy Bayesian computing for real parameter spaces, *Stat. Comput.* 16 (2008) 239–249.
- [44] R. Storn, K. Price, Differential evolution – a simple and efficient heuristic for global optimization over continuous spaces, *J. Glob. Optim.* 11 (1997) 341–359.
- [45] K.V. Price, R.M. Storn, J.A. Lampinen, *Differential Evolution: A Practical Approach to Global Optimization*, Springer 2005.
- [46] J.A. Vrugt, Markov chain Monte Carlo simulation using the DREAM software package: theory, concepts, and MATLAB implementation, *Environ. Model. Softw.* (2015)
- [47] E. Laloy, B. Rogiers, J.A. Vrugt, D. Mallants, D. Jacques, Efficient posterior exploration of a high-dimensional groundwater model from two-stage Markov chain Monte Carlo simulation and polynomial chaos expansion, *Water Resour. Res.* 49 (2013) 2664–2682.
- [48] A. Taflov, S.C. Hagness, *Computational electrodynamics: the finite-difference time-domain method*, Artech House, 1995.
- [49] K. Holliger, T. Bergmann, Numerical modeling of borehole georadar data, *Geophysics* 67 (2002) 1249–1257.
- [50] J. Irving, R. Knight, Numerical modeling of ground-penetrating radar in 2-D using MATLAB, *Comput. Geosci.* 39 (2006) 1247–1258.
- [51] J.R. Ernst, K. Holliger, H. Maurer, A.G. Green, Realistic FDTD modelling of borehole georadar antenna radiation: methodology and application, *Near Surface Geophysics*, 4, 2006. pp. 19–30.
- [52] S. Liu, Z. Zeng, L. Deng, FDTD simulations for ground penetrating radar in urban applications, *J. Geophys. Eng.* 4 (2007) 262–267.
- [53] A. Giannopoulos, Modelling ground penetrating radar by gprmax, *Constr. Build. Mater.* 19 (2005) 755–762.
- [54] N. Ahmed, T. Natarajan, K.R. Rao, Discrete cosine transform, *IEEE transactions on computers*, 100, 1974. pp. 90–93.
- [55] B. Jafarpour, V.K. Goyal, D.B. McLaughlin, William T. Freeman, Transform-domain sparsity regularization for inverse problems in geosciences, *Geophysics* 74 (2009) R69–R83.
- [56] P. Gilbert, Iterative methods for the three-dimensional reconstruction of an object from projections, *J. Therm. Biol.* 36 (1972) 105–117.
- [57] N. Ricker, The form and laws of propagation of seismic wavelets, *Geophysics* 18 (1953) 10–40.
- [58] H. Jeffreys, An invariant form for the prior probability in estimation problems, *Proceedings of the Royal Society of London. Series A, Mathematical and Physical Sciences*, 186, 1946. pp. 453–461.
- [59] A. Gelman, D.B. Rubin, Inference from iterative simulation using multiple sequences, *Stat. Sci.* 7 (1992) 457–472.
- [60] G. Vignoli, R. Deiana, G. Cassiani, Focused inversion of vertical radar profile (VRP) traveltime data, *Int. J. Non Linear Sci. Numer. Simul.* 77 (2012) H9–H18.

- [61] J. Sachs, M. Helbig, R. Herrmann, M. Kmec, K. Schilling, E. Zaikov, P. Rauschenbach, Trapped victim detection by pseudo-noise radar, Proceedings of the 1st International Conference on Wireless Technologies for Humanitarian Relief, 2011. pp. 265–272.
- [62] S. Chicarella, V. Ferrara, P. D'Atanasio, F.F.L. Pajewski, S. Pavoncello, S. Prontera, N. Tedeschi, A. Zambotti, Analyses and measures of GPR signal with superimposed noise, EGU General Assembly Conference Abstracts, 16, 2014. pp. 5387